The pattern and kinematics of deep deformation of 2012 Ahar-Varzaghan earthquake doublet (MW 6.4 and 6.2), a New seismotectonic interpretation

Mahnaz Nedaei *[1, 2], Hasan Alizadeh[1] , Mahdi Jahangiri[3]

1. Geology Department, Faculty of Basic Science, Payame Noor University (PNU), 19395-4697 Tehran, Iran
2 Board of Directors of Geological Society of Iran
3 Kavian Silise Kansar Co., Khoramdareh, Zanjan, Iran

Abstract

The 11th August 2012 Ahar-Varzaghan earthquake doublet Mw 6.4 and 6.2 occurred near the city of Ahar, northwest Iran, in a region where there was no major mapped fault or any well-documented historical seismicity. To investigate the active tectonics and the state of pre and post-seismic stress distribution of the source region, we applied a combination of Coulomb stress change, b-value mapping, and the Fry method. Inferred Coulomb stress field reveals the E–W-striking (dextral) fault responsible for the first event and the NNE–SSW-striking (sinistral reverse) fault for the second event. The high slip stress-released regions in the obtained b-value map and the dominant anisotropies of aftershocks on regional stress-parallel cross-sections achieved by the Fry method, together with the distribution of aftershocks mechanisms, merely highlight the particular wedge-shaped structures namely the rhombic structures. The clockwise block rotation about the vertical axis under the right-lateral regional shear between the Kura basin to the north and the Central Iranian Block to the south and NW-oriented coeval shortening leads to the formation of rhombic structures. The results of this study improve our understanding of the kinematics of active deformation in NW Iran and have important implications for seismic hazard assessment of the region and potential future failure area.

Keywords: Ahar-Varzaghan earthquake doublet; Coulomb stress change; Spatial b-value variation; Fry analysis; Rhombic structure.

1. Introduction

On August 11th 2012, a strong earthquake doublet (Mw 6.4 and 6.2) occurred in northwest Iran which affected both Varzaghan and Ahar and destroyed 20 villages and caused more than 300 deaths and 3000 injuries (Razzaghi and Ghafory-Ashtiany 2012). The 6.4 Mw Varzaghan–Ahar earthquake occurred at 12:23 UTC at a depth about 9 km. It was followed by a second event of comparable size, 6.2 Mw and at about 12 km depth only 6 km and 11 minutes apart. This doublet mainshocks were followed by three events of 5+ magnitude and many smaller aftershocks during a span of later few months. The biggest one occurred at 6:26 UTC on November 7th with 5.6 Mw. Institutions, providing global seismic moment tensors on an automatic base, determined consistently a nearly strike-slip mechanism on an east–west- or north–south-oriented plane for the first mainshock. For the second mainshock, they determined an either pure or oblique reverse mechanism with NNE–SSW-oriented planes (Fig. 1).

The main surface rupture associated with the doublet was about 12 km long (Blue line in the Fig. 1) extending from about 46.64° to 46.79° longitude as a nearly east–west right-lateral strike-slip fault with a maximum horizontal offset of ∼70 cm and a maximum vertical displacement of ∼25 cm showing frequent

left steps especially on its eastern section (Faridi and Sartibi 2012; Copley et al. 2014; Ghods et al. 2015). Two other independent segments of surface rupture were observed immediately after the earthquakes (See Fig. 2 for locations; Faridi and Sartibi 2012). The first was a reverse fault with ENE–WSW strike and about ∼1.3 km long south of Zaghan Abad village and the other was a N20E-striking fault, with a length of ∼2.4 km and a few centimetres of sinistral offset northwest of Guy Dareh village, beyond the eastern termination of the main rupture zone (Ghods et al. 2015).

The term doublet is usually used as a pair of earthquakes of similar magnitude being close in time and space and having some so far unknown physical connection between causative faults (Donner et al. 2015). The intracontinental earthquakes occur within collision zone in response to a generally uniform, compressional stress field associated with large-scale tectonic forces. Following Djamour et al. (2011), the collision between Arabia and Eurasia at northwest Iran, hosting the 2012 doublet, is purely intracontinental. Intracontinental earthquake doublets are rare and less studied. Therefore, the Ahar case is a good chance to learn more about the possible causes of intracontinental earthquake doublets.

----

*Corresponding author.
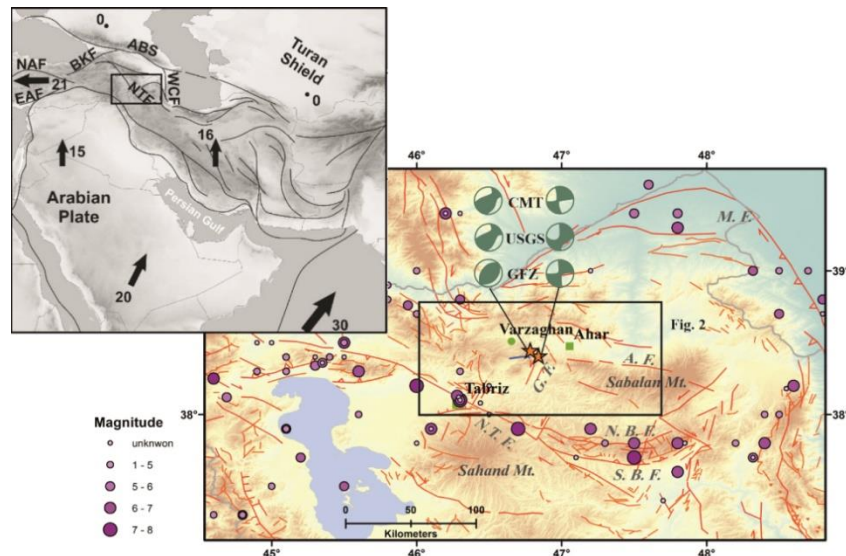E-mail address (es): m.nedaei@pnu.ac.ir

Fig 1. Inset: Outline map of the Arabia-Eurasia collision. Bold black arrows and associated numbers present plate velocities (Reilinger et al. 2006). Main figure: Active faults based on tectonic map of geological survey of Iran and recent works e.g., Copley et al. (2014), Donner et al. (2015), Ghods et al. (2015), Faridi et al. (2017), shown as red lines, the epicenters of great pre-historical and historical earthquakes of NW Iran, the epicenters and focal mechanism solutions of the Ahar-Varzaghan earthquake doublet (2012.08.11) plotted over the SRTM 90m DEM. Focal mechanism solutions of the earthquakes processed by international seismological centers show a nearly strike-slip mechanism on an east–west- or north–south-oriented plane for the first mainshock and an either pure or oblique reverse mechanism with NE–SW-oriented planes for the second mainshock. The Ahar-Varzaghan doublet mainshocks are shown as red stars. Only the E-W main surface rupture was marked as blue line and the two other surface ruptures couldn't be displayed with respect to the map scale. Violet circles present epicenters of pre-historical and historical earthquakes with magnitude above 5 from 2nd C. AD to 1965, modified by Ambraseys and Melville (2005). Abbreviations for faults are *AF*: Ahar fault, *GF*: Guyjabel Fault, *MF*: Moghan fault, *NBF*: North Bozgush fault, *NTF*: North Tabriz fault, *SBF*: South Bozgush fault, and for mountains are Sabalan Mountain and Sahand Mountain.

Earthquake doublets not only present particular challenges for seismic hazard assessment after a large event, but also provide insights into earthquake triggering (Ammon et al. 2008). For intracontinental earthquake doublets, various scenarios have been considered such as segmented seismicity (e.g., Daryono et al. 2012), Coulomb stress transfer on parallel faults (e.g., Astiz and Kanamori 1984; Horikawa 2001; Quintanar et al. 2004), the propagation of similar sized earthquakes along a large-scale fault zone (e.g., Bowman 1992; Bannister and Gledhill 2012), or elastic rebound of the second mainshock responding to the first mainshock (Chen et al. 2008).

Although historical seismicity in the northwest of Iran is mostly associated with the North Tabriz and the Bozqush faults, the doublet occurred in a region that is tectonically not well studied and faced with almost no historic or recent seismicity (Berberian and Yeats 1999; Iranian Seismological Center [IRSC]). The Ahar-Varzaghan doublet occurred in a region that has been characterized as having a low deformation rate and being bounded by deep-seated faults (Cisternas et al. 1997; Reilinger et al. 2006; Djamour et al. 2011). Such a characterization was consistent with the seismic record until 2012. Although seismic hazard information can be inferred from GPS velocities and related tectonic models, deformation of this type can be difficult to detect with typical regional geodetic networks (e.g.

Thatcher 2003). Tectonic activity in such regions of low tectonic and seismic activity rate resembles that of stable continental regions (Crone and Luza 1990; Crone et al. 1997; Wheeler and Crone 2001), where faults are characterized by relatively brief episodes of activity, separated by long periods of inactivity (Ghods et al. 2015). Long recurrence intervals and low long-term slip rates imply that geomorphic features associated with faults commonly are subtly expressed and poorly preserved. Therefore, detailed studies on the kinematic style in the current stress regime will be very crucial.

Coulomb stress change is one of a number of models related to the stress triggering in earthquakes (Hardebeck et al. 1998). Since the 1990s, the Coulomb stress change has been widely employed to probe the causality of triggering in several general types of studies: a) main shock-main shock triggering, b) main shock-aftershock triggering, and c) faults optimally oriented for failure. A large number of studies have investigated the Coulomb stress changes and earthquake interactions (e.g., King et al. 1994; Stein et al. 1994; Harris et al. 1995; Deng and Sykes 1997; Hardebeck et al. 1998; Harris 1998; Wang and Chen 2001; Parsons 2002; Wang et al. 2003; Lin and Stein 2004; Steacy et al. 2005; Lin et al. 2011; Mitsakaki et al. 2013; Yadav et al. 2012; Catalli et al. 2012; Hainzl et al. 2014; Wang et al. 2014; Bazoobandi et al. 2015; Sarkarinejad and Ansari 2014, 2015; Sharifi Teshnizi et al. 2021). There

are recent works of Ansari (2016) and Momeni et al. (2019) that have measured the Coulomb stress changes induced by the first shock on the nearby optimally oriented faults including the second causative fault. In both of them, first, the fault geometries of the Ahar-Varzaghan earthquake doublet had been defined or determined by other methods, then the Coulomb stress calculation was applied to investigate the stress distribution triggering the second mainshock and aftershocks (the "a" and "b" categories). Momeni et al. (2019) utilized the inversion nearfield strong-motion method to determine the geometry of the causative faults, but Ansari (2016) selected one of the nodal planes of each event as the causative faults without any explanation or documentation for such selection.

All studies performed on the Ahar-Varzaghan earthquake doublet based on different methods such as seismology, InSAR and field observations (e.g., Copley et al. 2014; Donner et al. 2015; Ghods et al. 2015; Ansari 2016; Momeni et al. 2019) agree on the E–W strike of the first mainshock fault plane, while there is no agreement on its dip, and the strike and dip of the second mainshock fault plane. In this paper, we used the static Coulomb stress changes in an innovative way to define the fault geometries of the 2012 Ahar-Varzaghan doublet. According to this, the Coulomb stress changes induced by regional stress have been implemented to find out optimally oriented nodal planes of the earthquake doublet for failure. Moreover, their interactions with the surrounding area were investigated by correlation between the epicentral distribution of aftershocks and the increased Coulomb stress zones. The comparable magnitudes of two mainshocks and their close spatial and temporal relationship suggest the structural dependence of causative faults. Accordingly, the spatial changes of b-value and Fry of the aftershocks on the stress-parallel cross-sections are estimated to find out whether the causative faults have a structural relationship or not. The current study aims to recognize the kinematics of active faulting in the area and consider them by a broader geodynamic framework. To these ends, combined methods have been applied to propose a kinematic model for NW Iran. Although many studies have investigated the Ahar-Varzaghan earthquake doublet, this paper clarifies deep structural aspects of the mainshocks and aftershocks shedding light on the pattern of active deformation in NW Iran that has not been mentioned yet. The results of this study have important implications for seismic hazard assessment of the region and potential future failure.

2.Tectonics setting

The Ahar-Varzaghan area is located in the northwestern block of Iran bounded on the west by the Borjomi Kazberg fault (BKF), on the south by the North Tabriz–Gailatu fault system (NTGS), and on the east by a series of N–S faults west of the Caspian Sea. At a regional scale, this fault-bounded area forms a triangular shape

(the area confined to the BKF, NTF and WCF in the gray inset figure of the Fig. 1) moving NNE with respect to Eurasia (e.g. Reilinger et al. 2006). Moreover, active deformation inside the triangular shaped area is accommodated along faults of different kinematics and orientations. The tectonics of northwest Iran are influenced by the northward motion of the Arabian indenter, the westwards extrusion of the Anatolian plate along the North- and East-Anatolian faults, and the reverse tectonics and subduction under the Greater Caucasus and the Apsheron–Balkhan sill, respectively, to the north (McKenzie 1972; Jackson 1992; Copley and Jackson 2006; Vernant and Chery 2006; Dabiri et al. 2011).

The 2012 doublet event happened within a pure intracontinental collision zone to the west of Sabalan and east of Sahand Quaternary volcanoes (See Fig. 1 for their locations). Before the 2012 earthquake sequence, our knowledge of active faulting in the region was limited to general information on geological maps (1:100 000 and 1:250 000 scales). No pre-earthquake active faulting is recognizable from available satellite images at the epicenter location and the contribution of the area to active deformation was unclear. The widespread seismic activity in the area is mostly localized on major block-bounding NW–SE right-lateral active faults such as the North Tabriz fault (NTF) which are responsible for historical and destructive earthquakes (Fig. 1; e.g. Innocenti et al. 1976; Pearce et al. 1990; Berberian 1997; Berberian and Yeats 1999). The sinistral NNE–SSW striking faults contribute to the accommodation of the N-S Holocene convergence between the Eurasian and Arabian plates in northwest Iran (Faridi et al. 2017). The Ahar-Varzaghan sequence, however, proved that there are hitherto unknown faults active north of the NTF.

The fault map of the region presented here (Figs. 1 and 2) is based on tectonic map of geological survey of Iran and recent works (e.g., Copley et al. 2014; Donner et al. 2015; Ghods et al. 2015; Faridi et al. 2017). The structural pattern of the area is defined by at least four distinct Quaternary fault sets trending E–W, WNW–ESE, NE–SW, and N–S (Fig. 2). Despite these main trending faults, at the epicenter location, no pre-earthquake strike-slip faulting is recognizable from available satellite images, and the destructive earthquakes were mostly located along deep-seated NW–SE right-lateral active faults. Large fold structures are rare in the area; the large one (~10 km length) is a SE-verging asymmetric Plio-Quaternary fault-related anticline trending NE, on the hanging wall of some NE–SW compressional faults at the north side of the surface rupture (Fig. 2). In the source region, the age of rock units changes drastically across the mapped surface rupture. The area to the north of the rupture line is mostly covered with Pliocene to Quaternary deposits (Fig. 2). On the southern side, the lithology is different and composed of Upper Cretaceous to Paleocene.
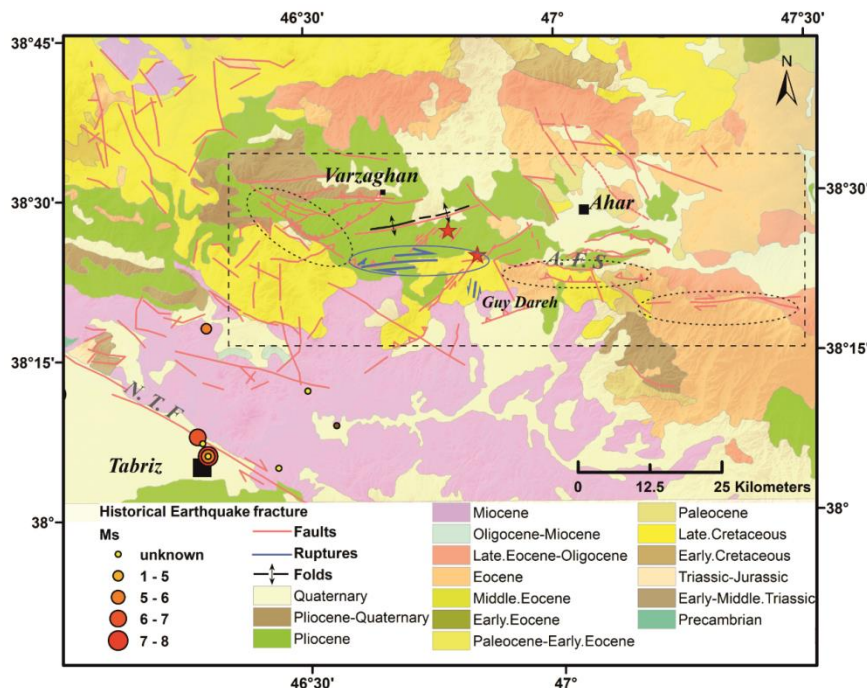
Fig 2. The general geological map is drawn according to GSI maps with scale 1:250.000. The topography is taken from SRTM data with a resolution of 90 m. See Figure 1 for the location. The Ahar-Varzaghan earthquake doublet is shown by red stars. Blue lines mark the surface ruptures. Red circles present epicenters of historical earthquakes. The dashed rectangle show the region of the *A.F.S* (Ahar Fault System) with the lack of seismicity in the past. Each segment of *A.F.S* is marked by a dotted ellipse. Blue ellipse shows the rupture segment of 2012.

The boundary between different lithologies of the southern and northern parts corresponds to a set of W- to NW-trending topographic ridges the middle sector (top) of which is affected by the 2012 rupture (see Faridi and Sartibi 2012; Copley et al. 2014; Fig. 2). On the southern side, the lithology is different and composed of Upper Cretaceous to Paleocene. The boundary between different lithologies of the southern and northern parts corresponds to a set of W- to NW-trending topographic ridges the middle sector (top) of which is affected by the 2012 rupture (see Faridi and Sartibi 2012; Copley et al. 2014; Fig. 2). Therefore, the E–W dextral fault reflects the geological boundary controlling the extent of both the Miocene and Pliocene-Quaternary sedimentary basins. This topography must have been built by a reverse fault transporting the older rocks on top of the younger ones in former times, which seems to be inactive at times (Donner et al. 2015). These reverse fault systems have formed a crustal weakness playing an important role in the later tectonic regime. More recently, the kinematic regime must have changed because shear strain is accommodated along right-lateral strike-slip fault (the main surface rupture) instead of contraction in the previously reverse faults at the source region. One possibility of this kinematic conversion is the geometry change in a way that the older reverse faults are connected at depth with a newly formed subvertical strike-slip fault, which ruptured the surface

during the Ahar-Varzaghan earthquake doublet (Donner et al. 2015).

At the western part of the main surface rupture, sets of N–S and NW–SE faults which have been less frequently expressed in previous researches, are observed. The fault-controlled geometry of bedding, by producing elongate topographic ridges, disrupts the NE-draining drainage patterns (Ghods et al. 2015). The eastern termination of the main surface rupture is also located in proximity of an active system of east–west-striking blind reverse faults (Copley et al. 2014). Farther east of 47.0° longitude, beyond the blind reverse fault system, an almost east–west-striking right-lateral strike-slip fault system is visible, as suggested by several dextral river offsets with on average 2 km displacement at about 47.4° longitude (Donner et al. 2015). The entire fault system, hereafter referred as Ahar fault system (the dashed rectangle in Fig. 2), clearly separates geological units older than Pliocene from younger ones and cuts bedding planes (Copley et al. 2014). The Ahar fault system, including the rupture segment of 2012, the reverse faults at its eastern and western terminations, and the strike-slip fault farther east, is strongly segmented, and depending on the fault segment geometry and the strain partitioning, exhibits different kinematics on different fault segments probably at different stages.

The transitions between the segments include stepovers (the dotted ellipses in Fig. 2) without distinct linking. Such an incomplete linkage may be an indication of a very young structure, which has not fully developed yet. The lack of seismicity in the past supports this assumption (Donner et al. 2015).

Previous works (i.e., Donner et al. 2015; Ghods et al. 2015) on distribution of aftershock mechanisms reveal more details about the structures within the area affected by the earthquake doublet. The aftershocks with strike-slip mechanisms (only considering events before November) are located along a subparallel linear at the northern edge of the sequence, all showing the same right-lateral character assuming the east–west-oriented planes to be the fault planes with coinciding deformation to the main rupture. The focal depths decreased at both ends of the aftershock zone especially in the western segment which was apparently separated from the main pattern of aftershock activity (Ghods et al. 2015). On November 7th, the largest aftershock with Mw 5.5 initiated a new subsequence of aftershocks implying north–south-oriented structures at the very western end of the sequence. The aftershocks with oblique reverse mechanisms were placed along the eastern and western end of the aftershock sequence on minor reverse faults subparallel to the minor surface ruptures. The geomorphology analyzed by geological maps (Geological Survey of Iran [GSI]), satellite images (Google Earth), and digital elevation data suggests the occurrence of reverse structures to the east and west of the sequence (Donner et al. 2015).

3. Methods and Materials

The slip occurring on faults (refered as *source faults*) during earthquakes, deforms the surrounding medium and changes its stress field. A method to estimate the change is the Coulomb static stress (Mitsakaki et al. 2013; Meier et al. 2014). The Coulomb stress changes can be derived from strain created by displacement of a source fault. Therefore, the shear and normal components of the stress change can be resolved on an area or on specified *receiver fault* planes. Receiver faults are planes with a specified strike, dip, and rake of slip vector (slickenline), on which the stresses are imparted by the source faults or tectonic regime. In other representation, the faults having optimal orientation with respect to the regional (also called tectonic) stress or the stress imparted by the source fault, and the assumed friction coefficient are suitable for sliding and could be as a receiver fault. The Coulomb failure stress change, ΔCFS, is defined as (Das and Scholz 1981; Stein et al. 1992; Harris 1998):

1) $\Delta\sigma_f(\Delta CFS) = \Delta\tau_s + \mu'\Delta\sigma_{n'}$

where $\Delta\tau_s$ is the change in shear stress on the receiver fault (set positive in the direction of fault slip), $\Delta\sigma_{n'}$ is the change in normal stress acting on the target fault (set positive for unclamping) and μ' is the effective coefficient of friction (Stein 1999; Toda 2008). The

shear stress increase or decrease is dependent on the position, geometry, and slip of the source fault and on the position and geometry of the receiver fault, including its rake. The normal stress change is independent of the slip vector rake of receiver fault. The parameter μ' is often called the apparent coefficient of friction and is intended to include the effects of pore pressure changes as well as the material properties of the fault zone (Harris 1998). Fault friction μ' is often inferred to be 0.4–0.8 for faults with little cumulative slip, which tend to be rough, and 0–0.4 for faults with great cumulative slip, which tend to be smooth (Ma et al. 2005). This parameter is typically found to be around 0.4 for strike-slip faults or faults with unknown orientation (Parsons et al. 1999; Sumy et al. 2014).

The positive ΔCFS (red regions in Coulomb map) indicates that the plane of interest was brought closer to failure; the negative ΔCFS (blue regions in Coulomb map) indicates that the plane of interest moved away from failure. Both increased shear and unclamping of faults promote failure (Stein et al. 1997; Harris and Simpson 1998; Parsons 2005; Toda et al. 2008; Aron and Hardebeck 2009). The Coulomb stress change depends on the geometry and slip of the earthquake, the geometry and sense of slip of the fault and the effective coefficient of friction (Stein et al. 1994).

There are two principal considerations of the Coulomb stress changes on receiver faults: stress changes on the specified receiver fault and stress changes on an optimally oriented receiver fault. The specified receiver faults rely on resolving stress changes on faults with known geometry (Ma et al. 2005; Hainzl et al. 2010). The optimally oriented receiver faults are determined by assuming that the earthquakes will be triggered only on those planes with maximum total Coulomb stress (King et al. 1994; Lin and Stein 2004; Ishibe et al. 2011; Catalli and Chan 2012).

The Gutenberg and Richter (1944) relation describes the number of earthquakes occurring in a given region as a function of their magnitude M as $\log N = a - bM$; where N is the cumulative number of earthquakes with magnitude equal to or larger than M, and a and b are real constants that may vary in space and time. The intercept "a" characterizes the general level of seismicity in a given area during the study period (i.e., the total number of earthquakes), while the slope "b" describes the relative size distribution of earthquakes. The parameter b can be estimated either by linear least squares regression or by maximum likelihood using the equation (Aki 1965; Ustu 1965; Bender 1983):

2) $b = \frac{1}{\overline{M} - M_{min}} \log e$

where $\overline{M}$ denotes the mean magnitude and M_{min} the minimum magnitude of the given sample. The determination of M_{min} relies on the magnitude distribution. Generally and practically, the minimum magnitude, M_{min}, is considered to be equal to the magnitude of completeness. The magnitude of

completeness, M_C, is determined by plotting the cumulative number of events as a function of magnitude. These plots are then fitted with a straight line and M_C is the level at which the data falls below the line.

General global average value of the *b* parameter, obtained by mixing different crustal rock volumes and different tectonic regimes, is close to unity. The *b*-value is believed to depend on the stress regime and tectonic character of the region (Allen et al. 1965; Mogi 1967; Hatzidimitriou et al. 1985; Tsapanos 1990). Statistically significant changes of *b*-values have been extensively studied for various stress regimes such as a subducting slab (Wyss et al. 2001), along fault zones (Wiemer and Wyss 1997) and in aftershock zones (Wiemer and Katsumata 1999). Based on seismicity studies, Schorlemmer and Wiemer (2005) suggested that the *b*-value can be used as a *stressmeter*. Regionally, changes in *b*-value are believed to be inversely related to changes in the stress level (Bufe 1970; Gibowicz 1973). Observations of local changes in *b*-values compared to the global average value, also reflect the effective stress (Scholz 1968). An increase in applied shear stress or effective stress results in a decrease in *b*-value (Wyss 1973; Urbancic et al. 1992). Low *b*-values have been correlated with areas of asperity, locked part of a fault where the nucleation of earthquakes is likely to happen (Schorlemmer et al. 2004; Tormann et al. 2012). High *b*-values have been correlated with the highest slip during large earthquakes (Sobiesiak et al. 2007; Görgün et al. 2009).

Fry method offers a quick and visually attractive approach to search for anisotropies in the distribution of point objects and specifically to investigate whether linear trends occur within a given data set. The technique was originally developed by Norman Fry (1979) to quantify finite strain based on a 2-D analysis of the nearest neighbors to a central reference point. There are so many researches applying Fry method for strain analysis (Bhattacharya and Weber 2004; Xypolias 2009). For the first time, Vearncombe et al. (1999) used the Fry method to assess distribution patterns of mineralization and potential controlling structures.

This method can be done manually by placing a tracing overlay with a coordinate origin and a pair of reference axes on top of a sketch or picture of the section. The origin is placed on a point and all other points are marked on the tracing paper. The tracing paper is then moved, without rotating the paper with respect to the section, so that the origin covers a second point, and each remaining point is again marked on the tracing paper. This procedure is repeated until the area of interest has been covered (Fry 1979). The resultant graph, commonly known as *Fry plot*, displays the position of each point relative to all other points viewed from a central position. If there are regular patterns in terms of spacing and orientation of points, the Fry plot will enhance such patterns allowing for an intuitive

visual analysis of their spatial controls. Fry analysis is an alternative to variography for directional studies. The orientations between every two points in a Fry plot can be represented in a rose diagram, which allows further analysis of spatial trends which are inherent, but not obvious, in the original Fry plot. If the original data set is a perfectly random point distribution, lines of all lengths will be homogeneously distributed in all directions. If the original distribution is not random, lines of particular lengths and/or orientations will occur more frequently displaying a fabric. The method yields interpretable results with small as well as large data sets (Vearncombe and Vearncombe 1999).

In earthquake studies by the Fry method, similar to what mentioned above, earthquake epicenters are marked on the scaled map with a pair of reference lines in N–S and E–W directions. The Fry method translates earthquake epicenters into a Fry plot by using every epicenter as an origin for translation. On a second tracing overlay but empty map, N–S- and E–W-trending reference lines are also drawn and an origin for translation is marked at the intersection of them. The origin in the second map is placed on top of one of the epicenters in the first map, while the reference lines in both maps are kept parallel. The positions of all the epicenters are recorded in the second map. The origin in the second map is then placed on top of a different epicenter in the first map, the reference lines in both maps are still kept parallel, and the positions of all the epicenters are recorded again in the second map. The procedure is repeated until all the epicenters in the first map have been used as the origin in the second map. In this way, the dominant trends in the earthquake epicenters appraising the trace of seismic faults can be shown in the rose diagram.

4. Results

In this research, recorded data by the Iranian Seismological Center (IRSC, irsc.ut.ac.ir) and also collected by the International Seismological Centre (ISC) from 2006 (once the data has been completely recorded) to 2018 with M_N (Nuttli magnitude) have been used. The Wells and Coppersmith (1994) empirical magnitude-area relations were implemented to estimate appropriate ruptures area of the first and second events. The characteristic of the earthquake doublet and four nodal planes given from the focal mechanism solutions of Global CMT and the moment tensor solutions determined by United State Geological Survey (USGS), are presented in Table 1. The rake angle of possible slip vectors obtained from waveform inversion method for the first and second mainshocks, are taken from GCMT and ISC. If there are a variety of different focal mechanisms within a region of uniform stress, determination of the principal stress directions and a measure of relative stress magnitudes is possible because on each fault plane, slip occurs in the direction of resolved shear stress (Bott 1959). Inversely, the stress state that produced the brittle structures can be partly

reconstructed knowing the direction and sense of slip on variably oriented fault planes. Each focal mechanism restricts the stresses generating the fault motion and is consistent with only a relatively limited family of stress tensors (Gephart and Forsyth 1984).

Table 1. The geometry of the Varzaghan-Ahar earthquake doublet nodal planes taken from GCMT and ISC.

Date	Time (UTC)	Lat (°N)	Lon (°E)	Depth (km)	M_W	Length (km)	Width (km)	Geometry of nodal planes			Different* combinations of nodal planes
								Strike (°)	Dip (°)	Rake (°)	
2012-08-11	12:23	38.33	46.83	9	6.4	24.5	10.1	A_1: 173	74	1	1#A_1B_1
								A_2: 82	89	164	2#A_1B_2
	12:34	38.39	46.74	12	6.2	19	11	B_1: 256	67	135	3#A_2B_1
								B_2: 7	49	31	4#A_2B_2

By inspecting the overlap of families of stresses associated with a number of focal mechanisms, the WinTensor program defines the range of stresses which may have acted over the region and combines the minimization of the misfit angle α and the maximization of the shear stress τ on every plane (Delvaux and Sperner 2003). The goal is to find the set of stresses that is most nearly consistent with all the observed focal mechanisms. The best-fitting regional stress tensor compatible with the majority of ISC collected earthquake focal mechanisms over the period of years was defined by WinTensor program (Table 2). The result is very similar to the stress field derived from kinematic-fault geological data by Ghods et al. (2015) and deduced the stress regimes from stress inversion of earthquake focal mechanisms by Afra et al. (2017).

Table 2. Principle stress direction

	σ_1	σ_2	σ_3
Trend	131	244	42
Plunge	4	86	2

The most important question concerning the Ahar-Varzaghan earthquake doublet is about the geometry and kinematics of the causative faults. In other words, we like to know which nodal planes would be the causative fault planes. With respect to the lack of seismicity and recognized active faulting in the Ahar area, there is no definitive answer to this question.

Earthquake focal mechanisms are defined by two orthogonal nodal planes, one of them being the plane that accommodated the slip during seismic activation (fault plane or causative fault) and the other being the auxiliary plane. In the absence of seismological or geological criteria, both nodal planes are potential slip planes that cannot be discriminated. The Coulomb static stress has been commonly used to determine the distribution of stress induced by an event, but for the first time, we applied it to realize the distribution of regional stress triggering an event on appropriate fault

(Nedaei and Alizadeh 2020). Theoretically, the optimally oriented receiver fault is determined by assuming that the earthquake will be triggered only on the fault plane with maximum total Coulomb stress. Inversely, the optimally oriented fault triggering the earthquake should have maximum Coulomb stress imparted by the regional stress (e.g., Toda et al. 2011). Therefore, the earthquake causative faults can be determined from nodal planes by resolving Coulomb stress on them with respect to the regional stress and selecting those on which the imparted Coulomb stress is maximum. In order to conduct this for the Ahar-Varzaghan earthquake doublet, four combinations of each pair of the nodal plane doublet were considered (Table 1; different cases in the last column).

The Coulomb stress change calculations were performed using the software Coulomb 3.3 (Toda et al. 2011). For all of the calculations of the Coulomb stress change, the shear modulus (G), 32×10^5 bar, Poisson ratio (ν) 0.25, Young modulus (E) 8×10^5 bar, effective coefficient of friction (μ') 0.4 (0.4 is often used) and the regional stress presented in Table 2, were used. The parameter values used in our calculations are based on the typical values proposed by Toda et al. (2011). The cases resulting in the greatest consistency with the inferred Coulomb stress field (both nodals lying on the warm colored regions in the Coulomb map), must be selected. By resolving Coulomb stress on all four cases, case number 2# and 4# represent more reliable results as both nodal planes were located in the positive ΔCFS area with greater than 0.5 bar ($\sim$0.5–$\sim$2.5 bars; Fig. 3b and 3d). The imparted Coulomb stress on case number 1# and 3# indicates that one of the nodal planes is situated in the negative ΔCFS regions (the cool colored regions in the Coulomb map) with smaller than -0.5 bar ($\sim$-0.5–$\sim$-2.5 bars; Fig. 3a and 3c). This means that the latter ones are not appropriate for earthquake triggering which caused them to be eliminated from the subsequent calculations. The aftershocks preferentially occur in the calculated stress increase and less likely in the calculated stress decrease areas (Parsons et al. 2014).
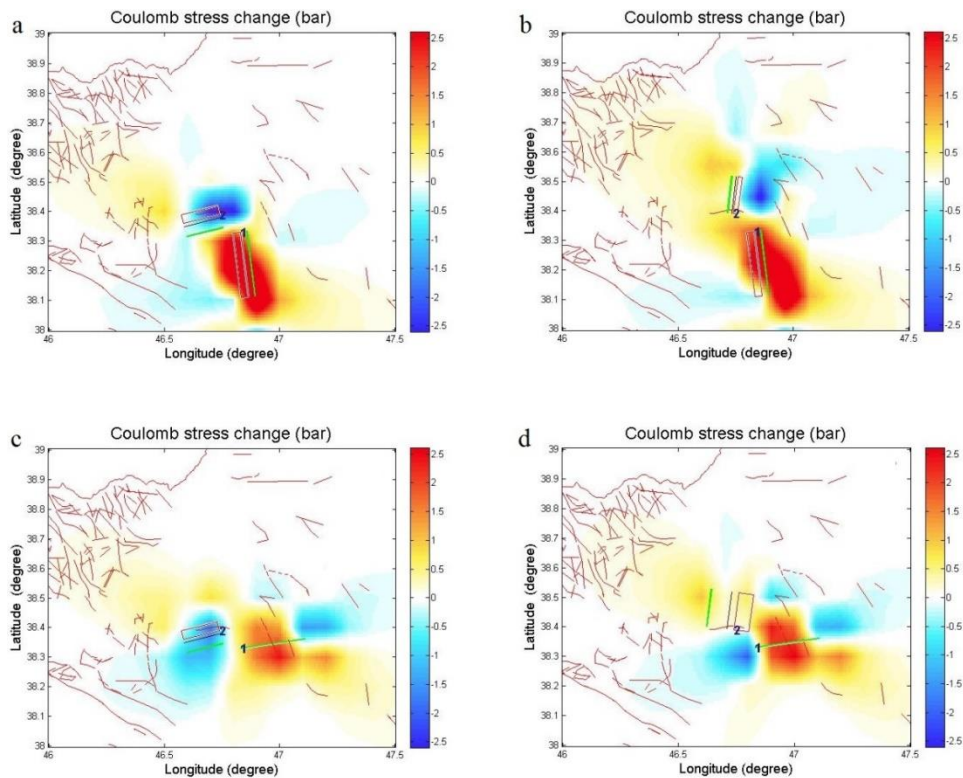
Fig 3. The Coulomb stress changes imparted by the regional stresses have been calculated with apparent coefficients of friction 0.4 for the various combinations of Ahar-Varzaghan earthquake doublet nodal planes. Figures a-d are related to case numbers 1-4 in the last column of Table 1, respectively. The warm colored areas represent the high Coulomb stress regions and the cool colored areas show the low Coulomb stress regions. Red rectangles show the hypothetical ruptures at focal depth based on Wells and Coppersmith relation and nodal planes geometry. Green lines represent the assumptive fault traces on the ground. Both nodal planes of case number 2 and 4 were located in the positive ΔCFS areas meaning they are appropriate for earthquake triggering. The imparted Coulomb stress on case number 1 and 3 show one of the nodal planes is situated in the negative ΔCFS making them not optimally oriented for failure.

Therefore, to assign whether case number 2# could be the earthquake doublet causative faults or case number 4#, the aftershocks with $M_N \geq 3$ by 3-month period following the doublet were plotted on inferred Coulomb stress map checking out which case is in good agreement with aftershock events distribution (Fig. 4). As is obvious from Figure 4, the spatial distribution of aftershocks clearly confirms the Coulomb stress pattern of case number 4#, namely, 82° for strike, 89° for dip and 164° for rake of the first mainshock causative fault with a dextral strike-slip mechanism and 7° for strike, 49° for dip and 31° for rake of the second mainshock causative fault with sinistral reverse mechanism. The hypocentral distribution of aftershocks on the σ_1- and σ_3-parallel (Table 2) cross-sections also coincides with the positive Coulomb stress lobes (located in the warm colored regions with greater than ∼0.5 bars in Fig. 5). The structural relationship between two causative faults and the Coulomb stress status triggering the earthquake sequence are explicit in the σ_1-parallel cross-section (AA' cross-section in Fig. 5). Several studies (e.g., Wiemer and Wyss 1997; Wiemer and Katsumata 1999; Wiemer et al. 2004; Tormann et al. 2012) compared the relative earthquake-size distribution or *b*-value cross-

section with the slip distribution during the earthquake sequence, suggesting that the high *b*-value regions correlate with the large slip stress-released regions. The postseismic slip regions highlight the barriers broken after the mainshock due to an increase in dynamic stress producing aftershocks (e.g. Scholz 2002). Therefore, to investigate postseismic stress-released regions or barriers at depth, we can visualize the *b*-value as a function of space in detail by projecting the aftershock hypocenters onto a vertical cross-section along desired strikes. In order to certify a homogeneous level of catalog completeness, the minimum magnitude of completeness (*Mc*) constraining the *b*-value map, should be estimated (Wiemer and Wyss 2000) or could be specified by homogeneity assumption of catalogue (Schorlemmer et al. 2004). We estimated *Mc* of the IRSC catalog from 2012.08.11 to 2013.02.10 (6-months duration of aftershock sequence) using the maximum curvature method estimated by the Zmap software to be 2.2 (Wiemer 2001). It means that above this magnitude, the catalog is complete. The spatial distribution of *b*-value was estimated by the maximum likelihood method using constant number (N=50) for aftershock sequence.
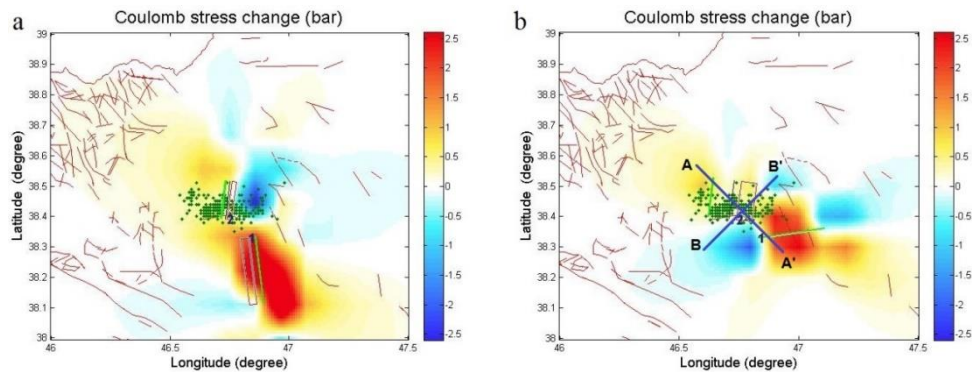
Fig 4. The aftershocks with magnitude greater than 3 (green dots) plotted over the Coulomb stress map for a) case number 2, and b) case number 4 (see figure 3 for more comparison). As is shown, most of the aftershocks have matched well with the high Coulomb stress area in case number 4 (b) but not in case number 2 (a). The distribution of aftershocks confirms case number 4 in Table 1 contains the causative faults of the Ahar-Varzaghan earthquake doublet. Blue lines in b are related to the presented cross sections in Figure 5.
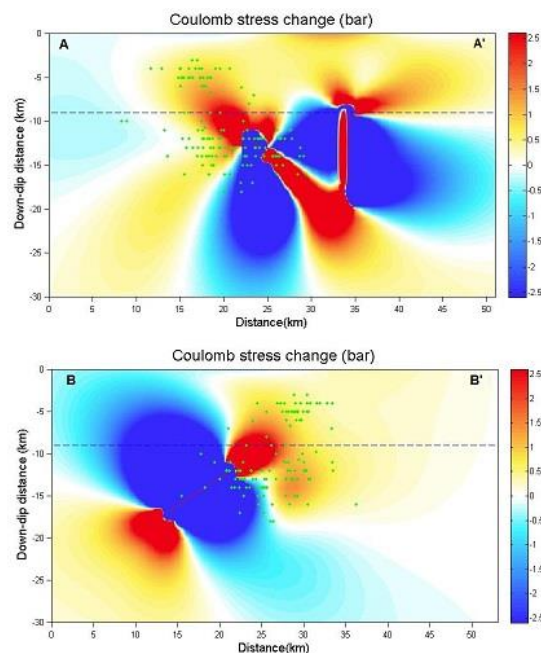

Fig 5. The Coulomb stress changes imparted by the regional stresses calculated along the σ_1-parallel cross-section (AA') and the σ_3-parallel cross-section (BB'). See Figure 4b for the orientation of cross-sections. Green dots represent the aftershocks. A characteristic wedge-shaped structure has been seen in the σ_1-parallel cross-section.

Based on this examination, we provided *b*-value spatial variation maps on three sections: along the trend of maximum regional stress (σ_1), along the trend of minimum regional stress (σ_3), and along the maximum elongational distribution of aftershocks subparallel to the main surface rupture (Fig. 6). The *b*-value cross-sections parallel to the trends of σ_1 and subparallel to the main surface rupture show high *b*-values larger than 1.2 at the area confined to the earthquake doublet source suggesting the high postseismic slip at stress-released

area (AA' and CC' cross-sections in Fig. 6). These regions showing characteristic wedge-shape structure possibly experienced preseismic stress-increased proposed as the barriers (Das and Henry 2003). In contrast, the high *b*-values regions on the σ_3-parallel cross-section up to 1.3 are fully consistent with the large slips across the main surface rupture along subparallel dextral faults (BB' cross-section in Fig. 6; e.g. Donner et al.2015).
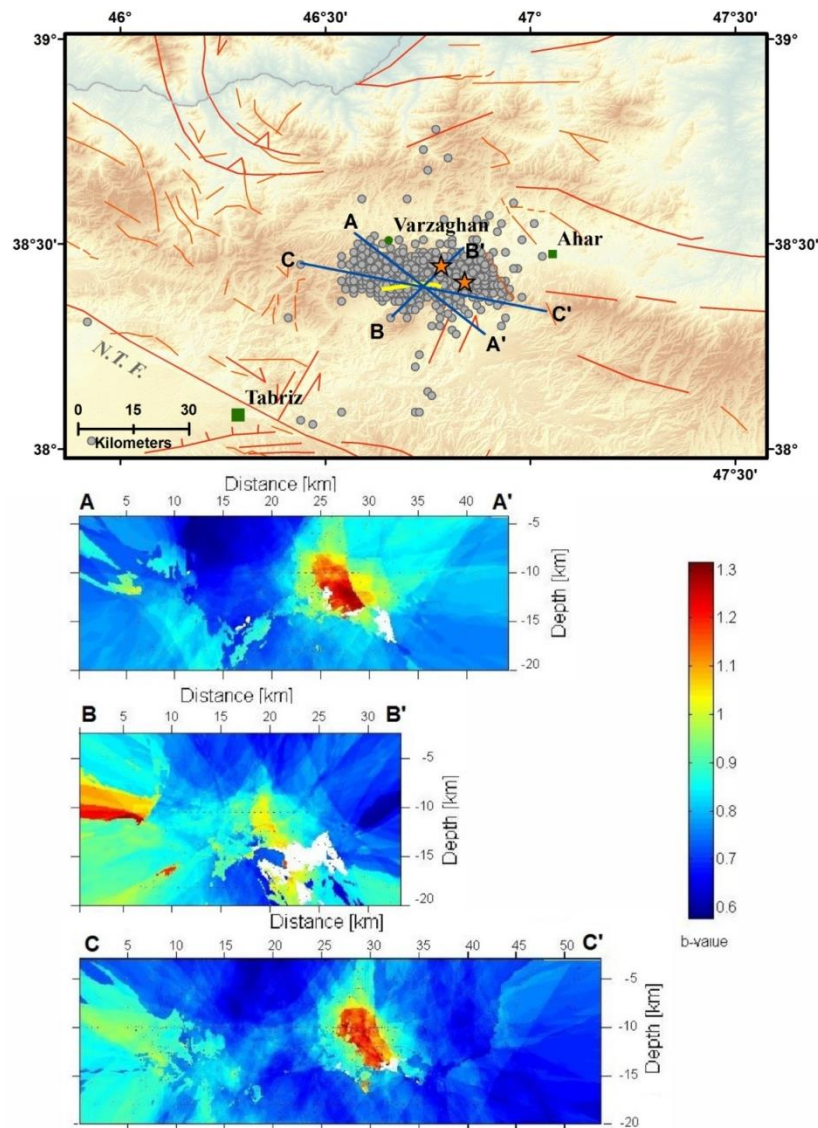
Fig 6. Insets: The spatial *b*-value cross-sections estimated for AA' parallel to the trend of σ_1, BB' parallel to the trend of σ_3 and CC' as the maximum elongation of aftershock distribution subparallel to the main surface rupture (yellow line in the main figure). Yellow to red areas represent high *b*-value due to numerous postseismic slips after the mainshocks. The high postseismic slip regions mark the stress-released areas namely barriers broken after the mainshocks. These regions show characteristic wedge-shape structure on AA' and CC' cross-sections. The high b-values regions on the σ_3-parallel cross-section (BB') are consistent with the large slips across the main surface rupture. Blue areas in the maps show low *b*-value regions. The location of the Ahar-Varzaghan earthquake doublet was marked by red stars.

Fry analysis can appraise characteristic spatial trends in the distribution of the earthquake epicenters which are inherent, but not obvious potentially occurred along the specific structures. In this way, the dominant trends in the earthquake epicenters can be shown in the rose diagram. For the first time, we utilized the Fry method on cross-sections to find out the spatial pattern of hypocentral distribution of aftershocks. Consequently, anisotropies in the distribution pattern of aftershocks specifically occurred along characteristic trends can be revealed. In so doing, the DotProc program v1.3 (Kuskov et al. 2001) has been implemented. In Fry

analysis using DotProc, a 2-D distribution pattern of data points is assessed by calculating connecting vectors between all points within a fixed X–Y reference frame. Fry plots were visualized by projecting the hypocentral distribution of aftershocks onto the σ_1- and σ_3-parallel vertical cross-sections using Zmap and ArcGIS softwares. Subsequently, the aftershocks were re-projected from a central point to reproduce distribution pattern of seismic events that exists in the original data set applying DotProc 1.3.

The existence of anisotropies represented as orientation and spacing of characteristic trends in the Fry plots can be further investigated with rose diagrams, in which a sub-set of vectors are plotted and assessed for preferential trends (Fig. 7). There are a few more frequent orientations in the rose diagram constructed on the σ_1-parallel cross-section of aftershock hypocenters, including two dominant subhorizontal trends, two more steepened but less dominant subvertical trends and one moderate-dip trend (AA' cross-section in Fig. 7). These trends demonstrate the existing anisotropies in the hypocentral distribution of aftershocks and disclose

concentration of aftershocks on dominant stress-releasing structures that are visible on the σ_1-parallel cross-section. The strongest trend in the plotted rose diagram on the cross-section parallel to the σ_3 trend, displays only one dominant subhorizontal anisotropy in hypocentral distribution of aftershocks representing an overall structure at the σ_3-parallel cross-section (BB' cross-section in Fig. 7). The resultants of Fry analysis on the stress-parallel cross-sections are in great compliance with the information obtained from *b*-value mapping on the same cross-sections.
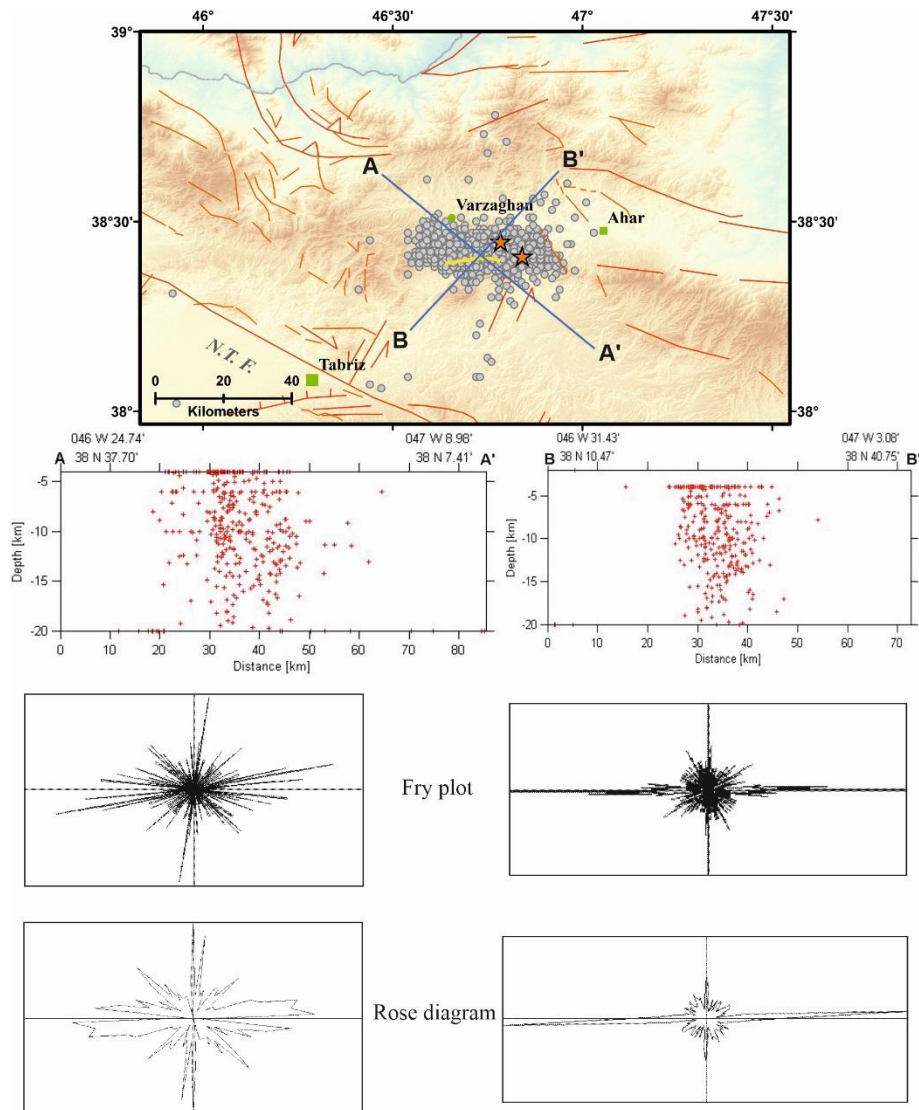

Fig 7. Insets: The distribution of aftershock events on the σ_1-parallel cross-section (AA') and the σ_3-parallel cross-section (BB'). The associated Fry plot and rose diagram are drawn under each cross section. Anisotropies in the rose diagrams reveal the dominant subhorizontal trends of aftershock concentrations on both cross-sections which is still much more intense on the σ_3-parallel cross-section (BB'). There is wedge-shaped anisotropy characterizing the concentration of aftershocks on σ_1-parallel cross-section. Yellow line in the main figure shows the main surface rupture. The location of the Ahar-Varzaghan earthquake doublet was marked by red stars.

5. Discussion

The first mainshock was located at 38.33° N and 46.83° E, near Guy Dareh village and the second one nucleated northwest of the first event and a few kms deeper, with epicenter at 38.39° N and 46.74°E near Golijeh village. The observed main surface rupture started in the west of the first mainshock and extended farther westward by curving to the south. It seems the extent of the surface rupture to the east intersects the location of the first mainshock epicenter. Evidently, the east–west-oriented surface rupture must have been produced by the first mainshock from profound depths upward with a westward migration. An important question concerning the second mainshock is whether it ruptured the same east–west oriented plane as the first mainshock or an oblique plane with north–south orientation (Fig. 2).

We applied the inferred Coulomb stress to find out which nodal planes are more probable for failure. Though each of the focal mechanism nodal planes of earthquake doublet theoretically could be the fault planes, those resulting in the greatest consistency with the inferred Coulomb stress field (lying on the positive ΔCFS regions of the Coulomb map) are the optimally oriented closer to failure. Among four combinations of each pair of nodal planes (Table 1), the imparted Coulomb stress on case number 1# and 3# show that one of nodal planes is situated in the negative ΔCFS (the cool colored regions in Fig. 3a and 3c) making them inappropriate for earthquake triggering and causing them to be excluded from the subsequent calculations. However, both nodal planes for case number 2# and 4# were located in the positive ΔCFS area (the warm colored regions in Fig. 3b and 3d). In the next step, the epicentral distribution of aftershocks with $M_N \geq 3$ plotted on the inferred Coulomb stress map confirms that case number 4# is the case composed of Ahar-Varzaghan earthquake doublet causative faults, namely, 82 ° strike, 89° dip and 164° rake for the first mainshock and 7° strike, 49° dip to the east and 31° rake for the second mainshock (Fig. 4b). This is in good agreement with the previous work of Donner et al. (2015) that considered the north–south-oriented fault for the second mainshock fault plane corroborated by November 7th aftershock subsequence.

Ansari (2016) selected the nodal plane with 84° strike, 84° dip, and 170° rake as the first mainshock fault plane and the 255° striking nodal plane with a dip of 63°, and a rake 134° as the second one. He did not provide any declaration about his assumption. Such an assumption about the characteristic of earthquake doublet (the fault geometries and the epicenter locations of the events) cannot kinematically justify two different mechanisms as strike-slip and reverse for the two adjacent subparallel causative faults. He also resolved the Coulomb model on the causative fault geometries and investigated the triggering of Coulomb stress change caused by Ahar-Varzaghan earthquake doublet. According to his examination, the second mainshock

and also post events were situated within the positive Coulomb stress zones induced by the first and second mainshock, respectively. In another study of this earthquake doublet, Momeni et al. (2019) retrieved the rupture process of both mainshocks by inverting the near-field strong motions data and using the elliptical subfault approximation method. Their calculations showed that the two earthquakes occurred on two distinct fault planes: the first mainshock has nucleated at a depth of ~8.5 km on an E–W striking fault (N88°E) that dips almost vertically (80°S). This earthquake exhibits a right-lateral strike-slip mechanism. The second mainshock occurred ~5 km to the west and 4 km to the north with respect to the hypocenter of the first mainshock, and at a depth of ~16.5 km on an ENE–WSW oriented fault plane (strike ~256°) with a dip of ~60° northward. They observed that the slip of the second event was essentially distributed on two distinct patches with pure right-lateral strike-slip and reverse mechanisms, respectively. The top of slip distribution of the second mainshock has stopped at a depth of ~8 km. Their obtained ENE–WSW striking fault plane for the second event (strike=256 and dip=60) is different from previous studies that have investigated the slip of this earthquake (e.g. Donner et al. 2015). From a rock mechanical perspective and by considering almost the same size of both earthquakes, the proposed kinematics by Momeni et al. (2019) for the second mainshock (first pure right-lateral then reverse mechanism) is impossible with respect to the geometry and right-lateral mechanism of the first mainshock fault plane. Moreover, the inversion method they utilized to determine the geometry of the causative faults was fundamentally different from our approach. They also calculated the Coulomb stress distribution triggering the second mainshock and aftershocks and showed that the rupture and the maximum slip of the second mainshock was controlled by the static Coulomb stress changes caused by the first mainshock.

After the occurrence of the first and the second mainshocks, the aftershocks migrated from the eastern to the western end of the sequence over time and spread over an area of about 20 km length in the E–W direction. From the Wells and Coppersmith (BSSA 1994) empirical magnitude-area relations, we estimated the size of the rupture plane for the first mainshock to be 24.5 × 10.1 km (Table 1) being in good agreement with the spreading length of aftershocks and the depth of the first mainshock hypocenter.

The postseismic stress-release (barrier) distribution at depth was also investigated by the *b*-value spatial cross-section. The *b*-value as a function of space was visualized by projecting the aftershock hypocenters onto the vertical cross-sections in a way that the high *b*-value regions correlate with the large slip regions. The *b*-value cross-sections parallel to the trends of σ_1 and subparallel to the main surface rupture show the characteristic wedge-shape high *b*-value regions at the earthquake

doublet source area (AA' and CC' cross-sections in Fig. 6). In contrast, the subhorizontal high b-value regions on the σ_3-parallel cross-section reveal the large postseismic slips across the main surface rupture along subparallel dextral faults (BB' cross-section in Fig. 6; e.g., Donner et al. 2015).

We also applied the Fry method on cross-sections, for the first time, to find out the spatial pattern of hypocentral distribution of aftershocks. Anisotropies in the distribution pattern investigated further by rose diagrams, revealed the specific trends of aftershock concentrations. The Fry plot and rose diagram constructed on the σ_1-parallel cross-section show more dominant subhorizontal anisotropy in the hypocentral distribution of aftershocks which is even much more intense on the σ_3-parallel cross-section (Fig 7). The σ_1-parallel cross-section also displays two other less frequent subvertical and steep orientations demonstrating wedge-shaped anisotropies that characterize the concentration of aftershocks on related stress-releasing structures (AA' cross-section in Fig 7).

The dominant anisotropies of Fry analysis on the stress-parallel cross-sections are in great compliance with the information obtained from b-value mapping on the same cross-sections except that based on the b-value calculation method, the high b-value regions show the continuous display against the discrete dominant trend in related rose diagrams. Compliance between anisotropies (concentrations) of aftershocks obtained by Fry method, and the high b-value regions (high slip stress-released regions), together with the distribution of aftershock mechanisms (i.e., Donner et al. 2015; Ghods et al. 2015), merely highlight the pattern and kinematics of deformation in a deep particular structure and put more interesting suggestions ahead. The subhorizontal trends unveiled on σ_3-parallel cross-sections in Fry analysis and b-value mapping represent the main strain-partitioning due to the large postseismic right-lateral strike-slip across the east–west-oriented fault planes at defined depth with coinciding deformation to the main rupture (BB' cross-sections in Figs. 6 and 7). The wedge-shaped structure revealed on σ_1-parallel cross-sections of Fry plot, b-value map (AA' cross-sections in Figs. 6 and 7), and also Coulomb stress cross-section (AA' cross-section in Fig 5) suggest stress-accumulation and -release on characteristic structure one side of which coincides to the east–west right-lateral strike-slip faults subparallel to the main surface rupture and the other side to the nearly north–south oblique reverse faults subparallel to the minor surface rupture confirmed by November 7th subsequence.

Rotation of rigid basal blocks about vertical axis in a bookshelf fashion, causes strike-slip faulting along the blocks. Movement along parallel basement strike-slip faults and the subsequent shortening of the overlying cover units, leads to the formation of typical wedge-shaped structures namely the rhombic structures (Koyi et al. 2016). They are similar to positive flower structures in appearance and development of positive topographies but are totally different in kinematics, genesis and structural extent from positive flower structures developed in transpressional zones. However, there are some fundamental differences between rhombic and positive flower structures (Koyi et al. 2016):

1. The sense of movement along the bounding strike-slip faults of rhombic structures is opposite to positive flower structures. In the rhombic structure, i.e., the two sinistral strike-slip fault segments overlapping in a left-step configuration, but in a positive flower structure, the strike-slip faults are in a left-step configuration, which need to be dextral, not sinistral.

2. Unlike in positive flower structures, where the thrusts dip towards each other, dip direction of thrusts in the rhombic structures can vary depending on which types of thrusts (fore- or back-thrusts) the strike-slip faults cross. In the rhombic structure, when strike-slip faults cross two adjacent fore-thrusts, the opposite thrusts dip in the same direction towards the hinterland; when strike-slip faults cross a fore- and back-thrust pair, the opposite thrusts dip in towards each other similar to regular flower structures or dip away from each other if the fore-thrust is located in the hinterland side of the back-thrust; and strike-slip faults cross-cutting two adjacent back-thrusts produce a rhombic structure where thrusts dip in the same direction towards the foreland.

There is a difference between the two structures in the relationship between the thrusts and strike-slip fault segments. This is because the thrusts within the rhombic structure are the result of regional shortening, not a local shortening due to strike-slip faulting as seen in the flower structures. In regular flower structures, thrusts form and are active only within the area bounded by the strike-slip faults. By contrast, the thrusts associated with the rhombic structures are not confined to the area defined by the strike-slip fault segments.

3. In regular flower structures, the thrusts form as a result of movement along the strike-slip faults and are active only within the area of the influence of the latter. This does not seem to be the case in rhombic structures since the thrusts are not a product of movement along the strike-slip faults, but have been formed due to the regional shortening. Thrusts are not confined to the area defined by the strike-slip fault segments and seem to cut/displace the strike-slip faults that bound the same rhombic feature.

The large right-lateral regional shear between the Kura basin to the north and the Central Iranian Block to the south (Vernant et al. 2004) causes the clockwise rotation of the basal fault-bounded blocks about vertical axis. This clockwise rotation of the blocks in NW Iran has been documented in many studies (e.g. Vernant et al. 2004; Masson et al. 2014; Khorrami et al. 2019). It seems the NNE–SSW striking left-lateral faults mentioned by Faridi et al. (2017) are the active basement faults playing an important role in

deformation of NW Iran (the dashed line with sinistral slip in Fig 8). The sinistral slip along these basement faults accommodates the Holocene shortening by clockwise rotation of the blocks. Interaction of the

NNE–SSW basement faulting and NW-oriented shortening (the σ_1 trend in Table 2) of the cover units, results in the formation of rhombic structures (Fig 8).
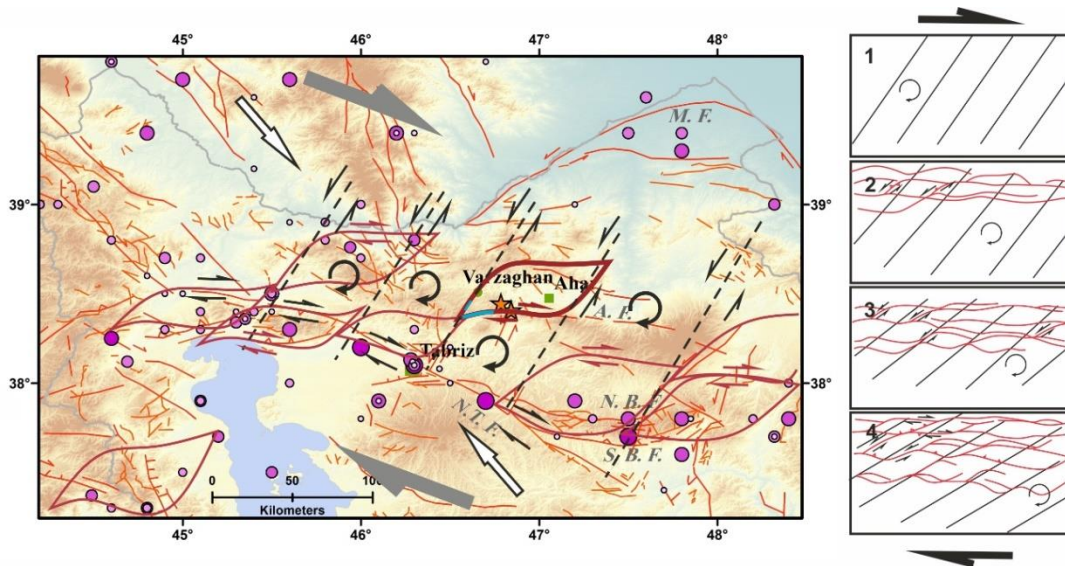

Fig 8. Simplified kinematic model of the study area plotted on Figure 1. This model presents formation of rhombic structures (dark red rhombuses) as a result of right-lateral shear between the Kura basin to the north and the Central Iranian Block to the south (Vernant et al. 2004) and NW-oriented coeval shortening (this study and Afra et al. 2017). The sense of shear in adjacent sides is opposite. The bold white arrows present the direction of present-day compressional stress. Black dashed lines represent clockwise rotating basal fault systems. The different stages of deformation have been presented according to Koyi et al. (2016) in the outside figure. Only the E-W main surface rupture was marked as blue line and the two other surface rupture couldn't be displayed with respect to the map scale. The position of historical earthquakes (violet circles) and the Ahar-Varzaghan earthquake doublet (red stars) concentrate at the rhombus sides. The mechanisms of Ahar-Varzaghan earthquake doublet, the clockwise rotation (Vernant et al. 2004; Masson et al. 2014; Khorrami et al. 2019) of NE-striking fault-bounded blocks, the accommodation of pre-historical and historical earthquakes along NTF, the existence of NW-striking normal faults west of Uremia lake are reasonable by this model.

The rhombic structures are bounded on two opposite sides by thrusts (or oblique thrusts) on and on the other two sides by strike-slip faults (oblique slip faults), which are partly overstepped. The E–W dextral strike-slip and NNE–SSW sinistral reverse faults which are two main fault sets reactivated or nucleated on closely spaced faults during the Ahar-Varzaghan earthquake doublet (i.e., the N–S sinistral fault northwest of Guy Dareh village; Faridi and Sartibi 2012; Ghods et al. 2015) fall into the rhombic pattern. In general, the thrust and strike-slip segments bounding the rhombic structures are oblique slip faults and the sense of lateral-slip in adjacent sides of the rhomb is opposite. Although in the model presented by Koyi et al. (2016), both fault sets may rotate with the progressive deformation to trends oblique to the bulk shortening direction, at the epicenter area only the NNE–SSW sinistral reverse faulting side of the rhombic structure has rotated with respect to the NW regional shortening. Their rotation leads to initiation of oblique rather than pure slip along them. The degree of oblique slip depends on the degree of their rotation.

Our resolved Coulomb stress on the causative faults of Ahar-Varzaghan earthquake doublet, confirms that the first mainshock is the E–W striking dextral fault and the second one has a sinistral reverse mechanism with the NNE–SSW strike. These two fault sets cannot be considered as Y and R1 Riedel shears for the following reasons:

1. The mechanism of the second mainshock is reverse with a minor component of left-lateral slip (See Fig 1), however, to be the R1 Riedel shear, it should have had a pure sinistral slip.

2. The geometrical relationship between the E–W dextral strike-slip fault and the NNE–SSW sinistral reverse fault does not match with the Y, R1, and T Riedel shears. The second fault sets should have been NW–SE or ENE–WSW oriented faults as supposed to be R1 or T Riedel shears, respectively.

3. The Ahar-Varzaghan earthquake doublet (Mw 6.4 and 6.2) separated in space by ~6 km and time by ~11 minutes. Such a similarly strong earthquake doublet only could be created by similar ranking faults, not by primary and subsidiary faults like Y and R1 Riedel shears.

4. Previous works (i.e., Donner et al. 2015; Ghods et al. 2015) reveal that the aftershocks with right-lateral strike-slip mechanisms were located along a subparallel linear to the main rupture, and confined to the ones with oblique reverse mechanisms placed along the eastern and western end of the sequence on minor reverse faults subparallel to the minor surface ruptures. This pattern is more consistent with rhombic structures rather than Riedel shear systems.

The rhombic structure implies similar sinistral reverse kinematics for other north-northeast-striking and dextral for east-striking faults distributed in the region, playing the role of linkage between the distinct NNE–SSW basement fault systems of NW Iran. In regions of low tectonic and seismic rate activity such as Ahar-Varzaghan area, the subset of active faults controlled by a regional complex structure like a rhombic structure, can be distinguished on the basis of their orientation with respect to the regional shear. An important implication in NW Iran is that all recognized faults and folds with NNE–SSW and E–W striking in the area are potentially hazardous in the present-day stress state and could produce damaging earthquakes, often in unexpected places (e.g., Crone and Luza 1990; Crone et al. 1997) although they may have remained aseismic for long periods in historic and modern times.

6. Conclusions

Accurate knowledge of geometry and kinematics of rare and less studied intracontinental earthquake doublets is crucial for characterization of dominant tectonic regime of the region and leads to a better understanding of the relevant geodynamic processes and a more realistic seismic hazard assessment. Therefore, the Ahar-Varzaghan case gives an excellent opportunity to investigate the active deformation and learn more about the possible causes of intracontinental earthquake doublets.

In this study, we investigated the Coulomb stress distribution triggering August 11th 2012 Ahar-Varzaghan earthquake doublet to understand the geometry and kinematics of the earthquake doublet as finding out which nodal planes are more probable for failure. Our results reveal the east–west-oriented dextral fault for the first mainshock and nearly the north–south-oriented sinistral reverse fault for the second mainshock. We also applied the spatial *b*-value change and Fry method on the regional stress-parallel cross-sections of aftershock hypocenters to suggest the postseismic stress-release distribution and the pattern of hypocentral distribution of aftershocks at depth. The high slip stress-released regions (barriers) obtained from *b*-value mapping are in good agreement with the dominant anisotropies (concentrations) of aftershocks in Fry analysis. This compliance, together with the distribution of aftershock mechanisms, merely highlight the pattern and kinematics of deformation in a deep particular rhombic structure. The E–W dextral strike-slip faults

subparallel to the main surface rupture and the NNE–SSW sinistral reverse faults subparallel to the minor surface rupture are the two main fault sets reactivated or nucleated during the Ahar-Varzaghan earthquake doublet falling into a typical structure known as the rhombic.

The right-lateral regional shear between the Kura basin to the north and the Central Iranian Block to the south causes the clockwise rotation of the blocks about vertical axis. The coeval block rotation and NW-oriented shortening lead to the formation of rhombic structures in NW Iran. Recognizing the pattern and kinematics of active deformation can help us to shed light on structural aspects of other block subjected to active deformation and answer some open questions on the geodynamics of northwestern Iran. The results of this study have important implications for seismic hazard assessment of the region and potential future failure area.

Aknowledgements

References

Afra M, Moradi A, Pakzad M (2017) Stress regimes in the northwest of Iran from stress inversion of earthquake focal mechanisms, *Journal of Geodynamics* 111:50-60.

Aki K (1965) Maximum likelihood estimate of b in the formula log N= a-bM and its confidence limits, Bull Earthq Res Inst, Tokyo Univ 43:237-239.

Allen CR, St. Amand P, Richter C, Nordquist J (1965) Relationship between seismicity and geologic structure in the southern California region, Bulletin of the Seismological Society of America 55:753-797.

Ambraseys NN, Melville CP (2005) A history of Persian earthquakes. Cambridge university press,

Ammon CJ, Kanamori H, Lay T (2008) A great earthquake doublet and seismic stress transfer cycle in the central Kuril islands, Nature 451:561-565.

Ansari S (2016) Co-seismic stress transfer and magnitude-frequency distribution due to the 2012 Varzaqan-Ahar earthquake doublets (Mw 6.5 and 6.4), *NW Iran, Journal of Asian Earth Sciences* 132:129-137.

Aron A, Hardebeck JL (2009) Seismicity rate changes along the central California coast due to stress changes from the 2003 M 6.5 San Simeon and 2004 M 6.0 Parkfield earthquakes, *Bulletin of the Seismological Society of America* 99:2280-2292.

Astiz L, Kanamori H (1984) An earthquake doublet in ometepec, guerrero, mexico, Physics of the earth and planetary interiors 34:24-45.

Bannister S, Gledhill K (2012) Evolution of the 2010–2012 Canterbury earthquake sequence, New Zealand *journal of geology and geophysics* 55:295-304.

Bazoobandi MH, Arian MA, Emami MH, Tajbakhsh GR, Yazdi A (2015) Geodynamics of Dikes in North of Saveh, *Open Journal of Ecology* 5(9), 452-459.

Bender B (1983) Maximum likelihood estimation of b values for magnitude grouped data, *Bulletin of the Seismological Society of America* 73:831-851.

Berberian M (1997) Seismic sources of the Transcaucasian historical earthquakes, Historical and prehistorical earthquakes in the Caucasus 28:233-311.

Berberian M, Yeats RS (1999) Patterns of historical earthquake rupture in the Iranian Plateau, *Bulletin of the Seismological society of America* 89:120-139.

Bhattacharya A, Weber K (2004) Fabric development during shear deformation in the Main Central Thrust zone, NW-Himalaya, India, Tectonophysics 387:23-46.

Bott MHP (1959) The mechanics of oblique slip faulting, Geological magazine 96:109-117.

Bowman JR (1992) The 1988 Tennant Creek, Northern Territory, earthquakes: A synthesis, *Australian Journal of Earth Sciences* 39: 651–669.

Bufe CG (1970) Frequency-magnitude variations during the 1970 Danville earthquake swarm, Earthquake Notes 41:3-7.

Catalli F, Chan C-H (2012) New insights into the application of the Coulomb model in real-time, *Geophysical Journal International* 188:583-599.

Chen H-Y, Lee J-C, Kuo L-C, Yu S-B, Liu C-C (2008) Coseismic Surface GPS Displacement and Ground Shaking Associated with the 2006 Pingtung Earthquake Doublet, Offshore Southern Taiwan, Terrestrial, *Atmospheric & Oceanic Sciences* 19.

Cisternas A, Philip H, Giardini D, Balassanian S (eds) (1997) Seismotectonics of the Mediterranean region and the Caucasus vol 28. *Historical and Prehistorical earthquakes in the Caucasus*,

Copley A, Faridi M, Ghorashi M, Hollingsworth J, Jackson J, Nazari H, Oveisi B, Talebian M (2014) The 2012 August 11 Ahar earthquakes: consequences for tectonics and earthquake hazard in the Turkish–Iranian Plateau, *Geophysical Journal International* 196:15-21.

Copley A, Jackson J (2006) Active tectonics of the Turkish-Iranian plateau, *Tectonics* 25.

Crone A, Machette M, Bowman J (1997) Episodic nature of earthquake activity in stable continental regions revealed by palaeoseismicity studies of Australian and North American Quaternary faults, *Australian Journal of Earth Sciences* 44:203-214.

Crone AJ, Luza KV (1990) Style and timing of Holocene surface faulting on the Meers fault, southwestern Oklahoma, *Geological Society of America Bulletin* 102:1-17.

Dabiri R, Emami M, Mollaei H, Chen B, Abedini M, Omran N, Ghaffari M (2011) Quaternary post-collision alkaline volcanism NW of Ahar (NW Iran): geochemical constraints of fractional crystallization process. *Geologica Carpathica* 62(6): 547-562

Daryono MR, Natawidjaja DH, Sieh K (2012) Twin-surface ruptures of the March 2007 M> 6 earthquake doublet on the Sumatran Fault, *Bulletin of the Seismological Society of America* 102:2356-2367.

Das S, Henry C (2003) Spatial relation between main earthquake slip and its aftershock distribution, *Reviews of Geophysics* 41.

Das S, Scholz CH (1981) Off-fault aftershock clusters caused by shear stress increase?, Bulletin of the Seismological Society of America 71:1669-1675.

Delvaux D, Sperner B (2003) New aspects of tectonic stress inversion with reference to the TENSOR program, Geological Society, London, Special Publications 212:75-100.

Deng J, Sykes LR (1997) Stress evolution in southern California and triggering of moderate-, small-, and micro-size earthquakes, *Journal of Geophysical Research:* Solid Earth 102:24411-24435.

Djamour Y, Vernant P, Nankali HR, Tavakoli F (2011) NW Iran-eastern Turkey present-day kinematics: results from the Iranian permanent GPS network, Earth and Planetary Science Letters 307:27-34.

Donner S, Ghods A, Krüger F, Rößler D, Landgraf A, Ballato P (2015) The Ahar-Varzeghan Earthquake Doublet (M w 6.4 and 6.2) of 11 August 2012: Regional Seismic Moment Tensors and a Seismotectonic Interpretation, *Bulletin of the Seismological Society of America* 105:791-807.

Faridi M, Burg J-P, Nazari H, Talebian M, Ghorashi M (2017) Active faults pattern and interplay in the Azerbaijan region (NW Iran), Geotectonics 51:428-437.

Faridi M, Sartibi A (2012) The Report of Ahar–Varzaghan Earthquake. Geological Survey of Iran, Tabriz Center (in Persian).

Fry N (1979) Random point distributions and strain measurement in rocks, Tectonophysics 60:89-105.

Gephart JW, Forsyth DW (1984) An improved method for determining the regional stress tensor using earthquake focal mechanism data: application to the San Fernando earthquake sequence, *Journal of Geophysical Research*: Solid Earth 89:9305-9320.

Ghods A, Shabanian E, Bergman E, Faridi M, Donner S, Mortezanejad G, Aziz-Zanjani A (2015) The Varzaghan–Ahar, Iran, Earthquake Doublet (M w 6.4, 6.2): implications for the geodynamics of northwest Iran, *Geophysical Journal International* 203:522-540.

Gibowicz SJ (1973) Variation of the frequency-magnitude relation during earthquake sequences in New Zealand, *Bulletin of the Seismological Society of America* 63:517-528.

Görgün E, Zang A, Bohnhoff M, Milkereit C, Dresen G (2009) Analysis of Izmit aftershocks 25 days before

the November 12th 1999 Düzce earthquake, Turkey, *Tectonophysics* 474:507-515.

Gutenberg B, Richter CF (1944) Frequency of earthquakes in California, *Bulletin of the Seismological Society of America* 34:185-188.

Hainzl S, Moradpour J, Davidsen J (2014) Static stress triggering explains the empirical aftershock distance decay, Geophysical Research Letters 41:8818-8824.

Hainzl S, Steacy D, Marsan S (2010) Seismicity models based on Coulomb stress calculations, Community Online Resource for Statistical Seismicity Analysis.

Hardebeck JL, Nazareth JJ, Hauksson E (1998) The static stress change triggering model: Constraints from two southern California aftershock sequences, *Journal of Geophysical Research:* Solid Earth 103:24427-24437.

Harris RA (1998) Introduction to special section: Stress triggers, stress shadows, and implications for seismic hazard, *Journal of Geophysical Research*: Solid Earth 103:24347-24358.

Harris RA, Simpson RW (1998) Suppression of large earthquakes by stress shadows: A comparison of Coulomb and rate-and-state failure, *Journal of Geophysical Research*: Solid Earth 103:24439-24451.

Harris RA, Simpson RW, Reasenberg PA (1995) Influence of static stress changes on earthquake locations in southern California, Nature 375:221-224.

Hatzidimitriou P, Papadimitriou E, Mountrakis D, Papazachos B (1985) The seismic parameter b of the frequency-magnitude relation and its association with the geological zones in the area of Greece, *Tectonophysics* 120:141-151.

Horikawa H (2001) Earthquake doublet in Kagoshima, Japan: Rupture of asperities in a stress shadow, *Bulletin of the Seismological Society of America* 91:112-127.

Innocenti F, Mazzuoli R, Pasquare G, Di Brozolo FR, Villari L (1976) Evolution of the volcanism in the area of interaction between the Arabian, Anatolian and Iranian plates (Lake Van, Eastern Turkey), *Journal of Volcanology and Geothermal Research* 1:103-112.

Ishibe T, Shimazaki K, Tsuruoka H, Yamanaka Y, Satake K (2011) Correlation between Coulomb stress changes imparted by large historical strike-slip earthquakes and current seismicity in Japan, Earth, planets and space 63:12.

Jackson J (1992) Partitioning of strike-slip and convergent motion between Eurasia and Arabia in eastern Turkey and the Caucasus, *Journal of Geophysical Research:* Solid Earth 97:12471-12479.

Khorrami F, Vernant P, Masson F, Nilfouroushan F, Mousavi Z, Nankali H, Saadat SA, Walpersdorf A, Hosseini S, Tavakoli P (2019) An up-to-date crustal deformation map of Iran using integrated campaign-mode and permanent GPS velocities, Geophysical *Journal International* 217:832-843.

King GC, Stein RS, Lin J (1994) Static stress changes and the triggering of earthquakes, *Bulletin of the Seismological Society of America* 84:935-953.

Koyi H, Nilfouroushan F, Hessami K (2016) Modelling role of basement block rotation and strike-slip faulting on structural pattern in cover units of fold-and-thrust belts, *Geological Magazine* 153:827-844.

Kuskov A, Mikhailov A, Dirks P (2001) DotProc v. 1.3. The analysis of 2–dimensional data sets, Computer shareware (http://dotproc fromru com).

Lin J, Stein RS (2004) Stress triggering in thrust and subduction earthquakes and stress interaction between the southern San Andreas and nearby thrust and strike-slip faults, *Journal of Geophysical Research:* Solid Earth 109.

Lin J, Stein RS, Meghraoui M, Toda S, Ayadi A, Dorbath C, Belabbes S (2011) Stress transfer among en echelon and opposing thrusts and tear faults: Triggering caused by the 2003 Mw= 6.9 Zemmouri, Algeria, earthquake, *Journal of Geophysical Research*: Solid Earth 116.

Ma KF, Chan CH, Stein RS (2005) Response of seismicity to Coulomb stress triggers and shadows of the 1999 Mw= 7.6 Chi-Chi, Taiwan, earthquake, *Journal of Geophysical Research*: Solid Earth 110.

Masson F, Lehujeur M, Ziegler Y, Doubre C (2014) Strain rate tensor in Iran from a new GPS velocity field, *Geophysical Journal International* 197:10-21.

McKenzie D (1972) Active tectonics of the Mediterranean region, *Geophysical Journal International* 30:109-185.

Meier MA, Werner M, Woessner J, Wiemer S (2014) A search for evidence of secondary static stress triggering during the 1992 Mw7. 3 Landers, California, earthquake sequence, *Journal of Geophysical Research*: Solid Earth 119:3354-3370.

Mitsakaki C, Rondoyanni T, Anastasiou D, Papazissi K, Marinou A, Sakellariou M (2013) Static stress changes and fault interactions in Lefkada Island, Western Greece, *Journal of Geodynamics* 67:53-61.

Mogi K (1967) Regional variations in magnitude-frequency relation of earthquakes, *Bull Earthq Res Inst* 45:313-325.

Momeni S, Aoudia A, Tatar M, Twardzik C, Madariaga R (2019) Kinematics of the 2012 Ahar–Varzaghan complex earthquake doublet (M w6. 5 and M w6. 3), *Geophysical Journal International* 217:2097-2124.

Nedaei M, Alizadeh H (2020) New insights into the 2017 Sefidsang earthquake by Coulomb stress change pattern and aftershock distributions: implication for active tectonics of NE Iran, *Geopersia*.

Parsons T (2002) Global Omori law decay of triggered earthquakes: Large aftershocks outside the classical aftershock zone, *Journal of Geophysical Research*: Solid Earth 107:ESE 9-1-ESE 9-20.

Parsons T (2005) Significance of stress transfer in time-dependent earthquake probability calculations, *Journal of Geophysical Research*: Solid Earth 110.

Parsons T, Segou M, Sevilgen V, Milner K, Field E, Toda S, Stein RS (2014) Stress-based aftershock forecasts made within 24 h postmain shock: Expected north San Francisco Bay area seismicity changes after the 2014 M= 6.0 West Napa earthquake, *Geophysical Research Letters* 41:8792-8799.

Parsons T, Stein RS, Simpson RW, Reasenberg PA (1999) Stress sensitivity of fault seismicity: A comparison between limited-offset oblique and major strike-slip faults, *Journal of Geophysical Research*: Solid Earth 104:20183-20202.

Pearce JA, Bender J, De Long S, Kidd W, Low P, Güner Y, Saroglu F, Yilmaz Y, Moorbath S, Mitchell J (1990) Genesis of collision volcanism in Eastern Anatolia, Turkey, *Journal of Volcanology and Geothermal Research* 44:189-229.

Quintanar L, Rodríguez-González M, Campos-Enríquez O (2004) A shallow crustal earthquake doublet from the Trans-Mexican Volcanic Belt (Central Mexico), *Bulletin of the Seismological Society of America* 94:845-855.

Razzaghi MS, Ghafory-Ashtiany M (2012) A preliminary reconnaissance report on August 11th, 2012, Varzaghan-Ahar twin earthquakes in NW of Iran, Report of International Association of Seismology and Physics of the Earth's Interior.

Reilinger R, McClusky S, Vernant P, Lawrence S, Ergintav S, Cakmak R, Ozener H, Kadirov F, Guliev I, Stepanyan R (2006) GPS constraints on continental deformation in the Africa-Arabia-Eurasia continental collision zone and implications for the dynamics of plate interactions, *Journal of Geophysical Research*: Solid Earth 111.

Sarkarinejad K, Ansari S (2014) The coulomb stress changes and seismicity rate due to the 1990 M W 7.3 Rudbar earthquake, *Bulletin of the Seismological Society of America* 104:2943-2952.

Sarkarinejad K, Ansari S (2015) Did the 1983 Charazeh earthquake trigger the destructive 1990 Rudbar earthquake?, *International Journal of Earth Sciences* 104:309-319.

Scholz C (1968) The frequency-magnitude relation of microfracturing in rock and its relation to earthquakes, *Bulletin of the seismological society of America* 58:399-415.

Scholz C (2002) The Mechanics of Earthquakes and Faulting. Cambridge University Press, Cambridge, 471 p.

Schorlemmer D, Wiemer S (2005) Microseismicity data forecast rupture area, Nature 434:1086-1086.

Schorlemmer D, Wiemer S, Wyss M (2004) Earthquake statistics at Parkfield: 1. Stationarity of b values, *Journal of Geophysical Research*: Solid Earth 109.

Sharifi Teshnizi E, Yazdi A, Rahnamarad J (2021) Geotechnical Characteristics of Liquefaction in Shahid-Rajaei Port Site (Bandar Abbas, Hormozgan Province) by Using GIS, *Geotechnical Geology* 17 (2), 613-626.

Sobiesiak M, Meyer U, Schmidt S, Götze HJ, Krawczyk C (2007) Asperity generating upper crustal sources revealed by b value and isostatic residual anomaly grids in the area of Antofagasta, Chile, *Journal of Geophysical Research*: Solid Earth 112.

Steacy S, Gomberg J, Cocco M (2005) Introduction to special section: Stress transfer, earthquake triggering, and time-dependent seismic hazard, *Journal of Geophysical Research:* Solid Earth 110.

Stein RS (1999) The role of stress transfer in earthquake occurrence, Nature 402:605-609.

Stein RS, Barka AA, Dieterich JH (1997) Progressive failure on the North Anatolian fault since 1939 by earthquake stress triggering, *Geophysical Journal International* 128:594-604.

Stein RS, King GC, Lin J (1992) Change in failure stress on the southern San Andreas fault system caused by the 1992 magnitude= 7.4 Landers earthquake, Science 258:1328-1332.

Stein RS, King GC, Lin J (1994) Stress triggering of the 1994 M= 6.7 Northridge, California, earthquake by its predecessors, Science 265:1432-1435.

Sumy DF, Cochran ES, Keranen KM, Wei M, Abers GA (2014) Observations of static Coulomb stress triggering of the November 2011 M5. 7 Oklahoma earthquake sequence, *Journal of Geophysical Research*: Solid Earth 119:1904-1923.

Thatcher W (2003) GPS constraints on the kinematics of continental deformation, *International Geology Review* 45:191-212.

Toda S (2008) Coulomb stresses imparted by the 25 March 2007 M w= 6.6 Noto-Hanto, Japan, earthquake explain its 'butterfly' distribution of aftershocks and suggest a heightened seismic hazard, Earth, planets and space 60:1041-1046.

Toda S, Lin J, Meghraoui M, Stein RS (2008) 12 May 2008 M= 7.9 Wenchuan, China, earthquake calculated to increase failure stress and seismicity rate on three major fault systems, *Geophysical Research Letters* 35.

Toda S, Stein RS, Sevilgen V, Lin J (2011) Coulomb 3.3 Graphic-rich deformation and stress-change software for earthquake, tectonic, and volcano research and teaching—user guide, *US Geological Survey open-file report* 1060:63.

Tormann T, Wiemer S, Hardebeck JL (2012) Earthquake recurrence models fail when earthquakes fail to reset the stress field, Geophysical research letters 39.

Tsapanos TM (1990) b-values of two tectonic parts in the circum-Pacific belt, *pure and applied geophysics* 134:229-242.

Urbancic T, Trifu C, Long J, Young R (1992) Space-time correlations ofb values with stress release, *Pure and Applied Geophysics* 139:449-462.

Ustu T (1965) A method in determining the value of b in a formula logn= a-bM showing the magnitude frequency for earthquakes, *Geophys Bull Hokkaido Univ* 13:99-103.

Vearncombe J, Vearncombe S (1999) The spatial distribution of mineralization; applications of Fry analysis, *Economic Geology* 94:475-486.

Vernant P, Chery J (2006) Low fault friction in Iran implies localized deformation for the Arabia–Eurasia collision zone, *Earth and Planetary Science Letters* 246:197-206.

Vernant P, Nilforoushan F, Hatzfeld D, Abbassi M, Vigny C, Masson F, Nankali H, Martinod J, Ashtiani A, Bayer R (2004) Present-day crustal deformation and plate kinematics in the Middle East constrained by GPS measurements in Iran and northern Oman, *Geophysical Journal International* 157:381-398.

Wang J, Xu C, Freymueller JT, Li Z, Shen W (2014) Sensitivity of Coulomb stress change to the parameters of the Coulomb failure model: A case study using the 2008 Mw 7.9 Wenchuan earthquake, *Journal of Geophysical Research*: Solid Earth 119:3371-3392.

Wang J-C, Shieh C-F, Chang T-M (2003) Static stress changes as a triggering mechanism of a shallow earthquake: case study of the 1999 Chi–Chi (Taiwan) earthquake, *Physics of the Earth and Planetary Interiors* 135:17-25.

Wang W-H, Chen C-H (2001) Static stress transferred by the 1999 Chi-Chi, Taiwan, earthquake: Effects on the stability of the surrounding fault systems and aftershock triggering with a 3D fault-slip model, *Bulletin of the Seismological Society of America* 91:1041-1052.

Wells DL, Coppersmith KJ (1994) New empirical relationships among magnitude, rupture length, rupture width, rupture area, and surface displacement, *Bulletin of the seismological Society of America* 84:974-1002.

Wheeler RL, Crone AJ (2001) Known and suggested Quaternary faulting in the midcontinent United States, *Engineering geology* 62:51-78.

Wiemer S (2001) A software package to analyze seismicity: ZMAP, *Seismological Research Letters* 72:373-382.

Wiemer S, Katsumata K (1999) Spatial variability of seismicity parameters in aftershock zones, *Journal of Geophysical Research*: Solid Earth 104:13135-13151.

Wiemer S, Toda S, Woessner J (2004) The Role of Stress in Causing High b-Value Regions in Aftershock Zones, AGUFM 2004:S13A-1034.

Wiemer S, Wyss M (1997) Mapping the frequency-magnitude distribution in asperities: An improved technique to calculate recurrence times?, *Journal of Geophysical Research*: Solid Earth 102:15115-15128.

Wiemer S, Wyss M (2000) Minimum magnitude of completeness in earthquake catalogs: Examples from Alaska, the western United States, and Japan, *Bulletin of the Seismological Society of America* 90:859-869.

Wyss M (1973) Towards a physical understanding of the earthquake frequency distribution, Geophysical *Journal International* 31:341-359.

Wyss M, Klein F, Nagamine K, Wiemer S (2001) Anomalously high b-values in the South Flank of Kilauea volcano, Hawaii: evidence for the distribution of magma below Kilauea's East rift zone, *Journal of Volcanology and Geothermal Research* 106:23-37.

Xypolias P (2009) Some new aspects of kinematic vorticity analysis in naturally deformed quartzites, *Journal of Structural Geology* 31:3-10.

Yadav R, Gahalaut V, Chopra S, Shan B (2012) Tectonic implications and seismicity triggering during the 2008 Baluchistan, Pakistan earthquake sequence, *Journal of Asian Earth Sciences* 45:167-178.